ACS APPLIED ENERGY MATERIALS

Article

Cite This: ACS Appl. Energy Mater. 2020, 3, 231−239

www.acsaem.org

"Breaking the O═O Bond": Deciphering the Role of Each Element in Highly Durable $CoPd_2Se_2$ toward Oxygen Reduction Reaction

Saurav Ch. Sarma,[†,‡] Vidyanshu Mishra,[†,‡] Vamseedhara Vemuri,[†,‡] and Sebastian C. Peter*[,†,‡]

[†]New Chemistry Unit, Jawaharlal Nehru Centre for Advanced Scientific Research, Jakkur, Bangalore 560064, India

[‡]School of Advanced Materials, Jawaharlal Nehru Centre for Advanced Scientific Research, Jakkur, Bangalore 560064, India

Supporting Information

ABSTRACT: In-depth insight into oxygen reduction reaction (ORR) electrocatalyst with high figures of merit (activity, stability, and selectivity) is highly crucial to rationally design electrocatalyst with a potential to replace state-of-the-art Pt/C. This work reports the synthesis of $CoPd_2Se_2$ nanoparticles that show remarkably high stability of 50000 electrochemical cycles toward ORR. Morphology of the particles is characterized using SEM and TEM microscopy techniques and simulated using Bravais−Friedel−Donay−Harker (BFDH) morphology calculation method. A deconvoluted approach was used to understand the role of each element in the compound. DFT calculation was performed to have an in-depth analysis of the active site. Co and Pd provided an active site for the O_2 adsorption and Pd dissociates the O═O bond. The back-donation of substantial electron density to the π^* antibonding orbital of the molecule expedites the 4e- reduction of O_2 throughout the entire potential range. During the electrochemical stability test, Se forms a protective layer and prevents the active Co and Pd sites from OH poisoning.

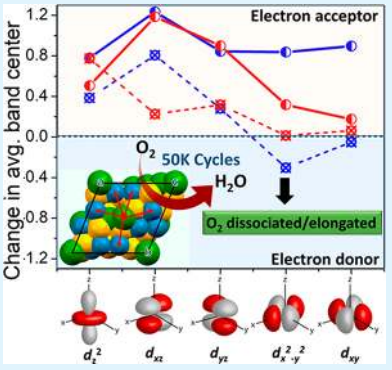

KEYWORDS: *oxygen reduction reaction, DFT calculation, d-band center, durability, BFDH morphology*

1. INTRODUCTION

The 21st century has witnessed a huge boom in the worldwide population, and as a consequence, the demand for energy increases exponentially. With decreasing fossil-fuel reserves, the demand can only be fulfilled with the contribution from renewable sources of energy. This has triggered the research on alternative energy sources such as fuel cells that can convert the energy stored in a chemical bond to electrical energy. However, the major constraint posed to the fuel cell emerges from the sluggish kinetics of the ORR catalyst that drops the cell potential owing to high overpotential of the ORR process. Achieving $4e^-$ reduction of O_2 to H_2O is highly desirable to obtain high energy efficiency. Besides, the catalyst should be able to sustain the activity for a prolonged period as well. Thus, activity, selectivity, and stability of electrocatalyst are the three figures of merit to classify the efficiency of an electrocatalyst. State-of-the-art ORR catalysts Pt/C and Pd/C possess high activity and selectivity; however, they degrade due to -OH poisoning within few thousand working cycles. The slowness of O/OH hydrogenation, during ORR, also impedes the adsorption of O_2 by occupying the adsorption sites with O/OH.[1] Low abundance of Pt further adds to the problem.[2−6] It is highly challenging to develop a catalyst that can mimic all of the desired properties of Pt/C and possess better stability.

Stability of an electrocatalyst is challenged by strong adsorption of intermediate species formed during the ORR process. Therefore, protection of active site by lowering the adsorption energy of the binding adsorbate is essential. This can be attained either by altering the pH of the electrolyte or through modifying the catalyst surface.[7−9] Since adsorption of charged species is highly potential-dependent, the use of alkaline medium is preferred in industry and space programs.[10−13] However, this does not entirely resolve the stability issue. Consequently, a secondary element is required that can protect the active site from degradation.[14−17] Pd has a high surface energy of around 1.43 J/m^2. This results in the agglomeration of Pd nanoparticles which then decreases the activity of the catalysts.[18] Selenium, because of its low surface energy of 0.10 J/m^2, forms a thin layer on the surface and justifies the role of the secondary element by preventing oxidation of the transition metal up to potentials of about 0.8−0.9 V vs RHE in the alkaline medium.[19,20] This has been explained in our previous work, wherein we proved that during the electrochemical ORR measurements on $Pd_{17}Se_{15}$ catalyst in 0.1 M KOH (pH ∼ 13), Se forms a protective oxide layer and prevents the metal active sites from oxidative leaching. Thus, the active sites remain protected for a prolonged time.[20] Thus, chalcogenides represent a potential alternative to the Pt-based catalyst in terms of stability. A group of chalcogenide-based catalysts such as $PtTe_2$,[21] NiS_2,[22] CoS_2,[23] $Co_{1-x}S$,[24] Co_3S_4,[25] Co_9S_8,[26] $CoSe_2$,[27−29] Co_7Se_8,[30] ReS_2,[31] MoS_2,[32−34] and WS_2[35,36] are reported for promising applications toward electrochemical reactions. Another major issue with Pd is the

Received: July 18, 2019
Accepted: December 2, 2019
Published: December 2, 2019

DOI: 10.1021/acsaem.9b01400
ACS Appl. Energy Mater. 2020, 3, 231−239

formation of significant amounts of H_2O_2, which is known to corrode the catalyst surface.[37]

Having understood the issue of durability in our previous work,[20] we tried to understand other figures of merit such as selectivity and activity in this work. ORR process can yield either H_2O or H_2O_2 formed via $4e^-$ or $2e^-$ transfer, respectively. Product formed during the reaction is mainly determined by the adsorption energy with which an oxygen molecule is bonded to the catalyst surface and the ability of the catalyst to dissociate the O═O bond. Pt/TiC was observed to exhibit 4 times better activity than Pt/C due to its ability to easily dissociate the O═O bond.[38] There have been several reports suggesting that the adsorption energy of O_2 on the surface should neither be too strong that the surface gets poisoned nor be too weak that the reaction does not progress further.[39,40] There are two types of adsorption modes reported in the literature: end-on mode (Pauling model), where O_2 adsorbs through a single bond on the catalyst surface, and the side-on mode (also known as Yeager model), where an O_2 molecule forms a bridge-like adsorption with two bonds interacting with two sites.[41] Choi et al. proposed that side-on adsorption of O_2 forms H_2O and end-on adsorption of O_2 can form either of the products. Dissociative adsorption of O_2 requires adjacent metals for the dissociation to take place.[42,43] H_2O can also form due to chemical decomposition of H_2O_2, which also requires secondary metal. However, the preferred product is H_2O to maximize the energy conversion efficiency of the process.

In this work, $CoPd_2Se_2$ chalcogenide nanoparticles have been synthesized that show high activity and stability for 50000 electrochemical cycles and has exclusive selectivity toward H_2O over a wide-potential range. The catalyst retains its selectivity toward H_2O, better than Pt, over a prolonged time. The compound also exhibits high methanol-tolerance activity. We performed a comprehensive analysis to understand the role of Co, Pd, and Se toward these remarkable figures of merit. Cobalt and palladium in this work provide an active site for the dissociative process. A small amount of selenium, because of its low surface energy, forms an overlayer on the surface of the catalyst and protects Co and Pd active sites from degradation, thus maintaining its durability toward the reaction for 50000 cycles.

2. EXPERIMENTAL PROCEDURES

2.1. Chemicals. Palladium acetylacetonate ($Pd(C_5H_7O_2)_2$, 99%), cobalt acetylacetonate ($Co(C_5H_7O_2)_2$, 99%), selenous acid (H_2SeO_3, 98%), trioctylphosphine ($P(C_8H_{17})_3$, 90%), and oleylamine ($C_{18}H_{35}NH_2$, 70%) were purchased from Sigma-Aldrich. All of the reagents were used without further purification. Milli-Q water (18.2 MΩ cm) was used throughout the synthesis and electrochemical measurements.

2.2. Synthesis of $CoPd_2Se_2$. $CoPd_2Se_2$ nanoparticles were synthesized by colloidal synthesis method. A 0.1 mmol amount of $Pd(acac)_2$, 0.1 mmol of H_2SeO_3, and 0.07 mmol of $Co(acac)_2$ were mixed together in 25 mL of oleylamine in a 50 mL two-necked round bottom (RB) flask. A 1000 μL aliquot of trioctylphosphine was then added to the solution. The RB flask was then fitted to a condenser, vacuumized, and purged with Ar gas. It was then heated at 220 °C for 3 h. The product obtained was repeatedly washed with a hexane−ethanol mixture for several times and then dried in a vacuum oven at 60 °C for 6 h.

2.3. Characterization. The PXRD measurements at room temperature were carried out on a Rigaku miniflex X-ray diffractometer with Cu Kα as the X-ray source (λ = 1.5406 Å). The instrument is equipped with a position sensitive detector in the angular range $20° \leq 2\theta \leq 90°$ with the step size 0.02° and scan rate of 1 s/step calibrated against corundum standard. The experimental patterns were compared to the pattern simulated from the database.

In order to extract structural information from the diffraction data, we used the Rietveld method as implemented in the FullProf suite program. Quantitative microanalyses on all of the samples were performed with a FEI NOVA NANOSEM 600 instrument equipped with an EDAX instrument. Data were acquired with an accelerating voltage of 20 kV and a 100 s accumulation time. The EDAX analysis was performed using P/B-ZAF standardless method (where Z = atomic no. correction factor, A = absorption correction factor, F = fluorescence factor, and P/B = peak to background model) on selected spots and points. TEM images and selected area electron diffraction patterns were collected using a JEOL JEM-2010 TEM instrument, and color mapping was done in TECHNAI. The samples for these measurements were prepared by sonicating the nanocrystalline powders in ethanol and drop-casting a small volume onto a carbon-coated copper grid. XPS measurement was performed on an Omicron Nanotechnology spectrometer using a Mg Kα (λ = 1253.6 eV) X-ray source with a relative composition detection better than 0.1%.

Pd *K*-edge EXAFS measurements of the catalysts were carried out in transmission mode at the PETRA P65 beamline of DESY.[44] Pellets for the measurements were made by homogeneously mixing the sample with an inert cellulose matrix to have an X-ray absorption edge jump close to one. Standard data analysis procedure was used to extract the EXAFS signal from the measured absorption spectra. Background subtraction, normalization, and alignment of the EXAFS data were performed by using the ATHENA software.[45] Theoretical EXAFS models were constructed and fitted to the experimental data in ARTEMIS. EXAFS data of the catalyst materials were fitted simultaneously with *k*-weights of 1, 2, and 3. The S_0^2 value was fixed to 1 prior to EXAFS fitting. The data were Fourier transformed in the range of 4−13.8 $Å^{-1}$. They were then fitted in *R* space between 1 and 3 Å for all samples. The fitting parameters were bond-length change between atoms (ΔR), change in energy scale between data and theory (ΔE_0), and mean-square displacement of the bond length (σ^2), while the coordination numbers (CNs) were fixed from crystallography data of $CoPd_2Se_2$.

2.4. Electrochemical Studies. All of the electrochemical measurements were carried out using a CHI 760E electrochemical workstation with three electrode channels at room temperature. A conventional three electrode setup consisting of a glassy carbon (GC) (having diameter of 3 mm) as working electrode, platinum wire as counter electrode, and Hg/HgO (MMO) as reference electrode was used. Before all of the measurements, the electrolyte was deaerated with continuous purging of nitrogen gas for 30 min. The catalyst ink was prepared by dispersing 1 mg of catalyst in 200 μL of mixed solvent solution (IPA:H_2O = 1:3 (v/v)). Nafion solution (5 wt %, Sigma-Aldrich) is diluted with isopropyl alcohol (IPA) to 0.05 wt %. From the prepared catalyst ink, 5 μL of the slurry was drop-cast on GC electrode. Upon drying, a 5 μL aliquot of 0.05 wt % Nafion solution has been added to the drop-cast electrode and dried overnight in air. The GC electrode was polished with 0.05 μm alumina slurry and washed several times with distilled water prior to the deposition of catalyst slurry. Commercial Pd/C and Pt/C (20 wt %, Sigma-Aldrich) (with the same Pd/Pt loading on the electrode) were used for comparison of activity with the same loading as that of the synthesized catalysts. The commercial catalysts were tested by keeping all of the experimental conditions the same as in $CoPd_2Se_2$. Chronoamperometric (CA) measurements were performed in 0.1 M KOH electrolyte solution. Linear-sweep voltammetry (LSV) was recorded with a sweep rate of 5 mV/s in 0.1 M KOH electrolyte solution under steady state conditions. Tafel plots (TPs) were derived from LSV measurement. Accelerated degradation test (ADT) was performed with graphite rod (purity > 99.9%, Sigma-Aldrich) to avoid Pt dissolution. Stability tests were carried out at a scan rate of 100 mV s^{-1} and within a potential window of 0.4−0.9 V vs RHE. The potential window for the stability test was selected on the basis of previous literature.[46−48] After every 2000 potential cycles, LSV graphs

DOI: 10.1021/acsaem.9b01400
ACS Appl. Energy Mater. 2020, 3, 231−239

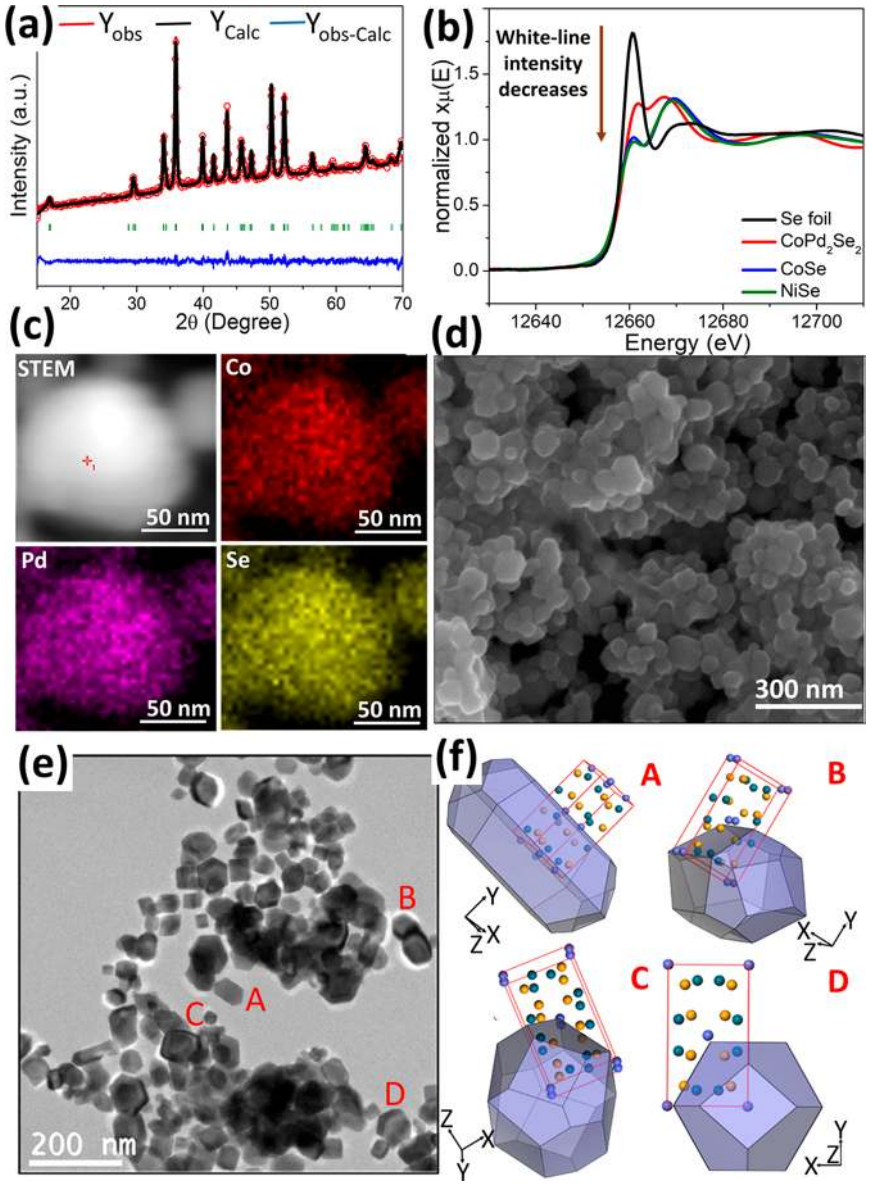

Figure 1. (a) Rietveld refinement of the powder XRD pattern of as synsthesized $CoPd_2Se_2$ nanoparticles. (b) Se *k*-edge XANES spectra, (c) elemental mapping, and (d) SEM image of $CoPd_2Se_2$ nanoparticles. (e, f) Morphology of the $CoPd_2Se_2$ nanoparticles compared with BFDH generated morphology of $CoPd_2Se_2$. Simulated morphology confirms that particles have the same morphology, oriented along different directions as denoted by *x*-, *y*-, and *z*-axes. Particles are marked as A, B, C, and D, and their corresponding simulated morphologies are presented alongside.

were recorded to check the stability of the catalyst. Selectivity toward H_2O, before and after 1000 cycles, was checked using RRDE electrode with 4 mm diameter and keeping all other experimental conditions similar. All of the electrochemical data, presented in this work, are referenced to RHE scale.

2.5. Theoretical Calculation. DFT calculations were performed using PWSCF v.5.1 code embedded in the Quantum Espresso suite for quantum simulation of materials.[49] The PWSCF calculations were performed using generalized gradient approximation (GGA) with PBE[50] exchange−correlation functional and ultrasoft pseudopotential. Kinetic energy (E_k) cutoff for the wave functions of 35.0 Ry was used to truncate the plane-wave basis. Furthermore, Gaussian smearing was used with a degauss value of 0.005 Ry. Systems were relaxed until the Hellmann−Feynman forces on each atom are in the order of 10^{-2}–10^{-3} eV/Å. The calculated Fermi energy (E_F) was set to zero for all of the DOS plots. A vacuum of 10 Å was used to avoid any interaction among the slabs.

Systematic density functional theory was carried out to determine the interaction between the adsorbate and adsorbant. We applied the d-band model proposed by Hammer and Nørskov.[51] The d-band center (ε_{av}) is given by the following relation in this model:

$$\varepsilon_{av} = \frac{\int_{-\infty}^{E_f} E\rho(E)\,dE}{\int_{-\infty}^{E_f} \rho(E)\,dE}$$

where ρ is the projected density of d-states of surface atoms, E is the energy, and E_F is the Fermi level.

Change in the average band center was calculated using the following formula:

$$\Delta = \varepsilon_{av,initial} - \varepsilon_{av,final}$$

where $\varepsilon_{av,initial}$ and $\varepsilon_{av,final}$ represent the average band center before and after the adsorption of O_2 molecule.

3. RESULTS AND DISCUSSION

3.1. Crystal Structure. The crystal structure of $CoPd_2Se_2$ is isotypic to K_2ZnO_2[52] crystallizing in the orthorhombic

DOI: 10.1021/acsaem.9b01400
ACS Appl. Energy Mater. 2020, 3, 231−239

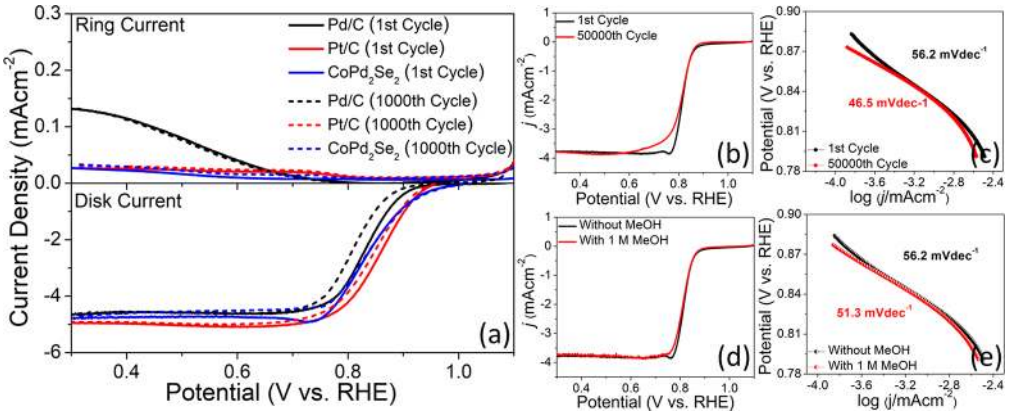

Figure 2. (a) Comparison of RRDE polarization curve of Pd/C (20 wt %), Pt/C (20 wt %), and $CoPd_2Se_2$ recorded at 1600 rpm in O_2-saturated 0.1 M KOH. Disk current represents current due to reduction of O_2 to H_2O and H_2O_2, and ring current signifies current due to oxidation of H_2O_2. (b) Polarization curve of the catalyst before and after ADT test showing negligible shift in the onset potential. (c) Comparison of the Tafel slope before and after the ADT test shows a similar Tafel slope. Negligible change in the (d) polarization curve and (e) Tafel slope of the catalyst in the presence of methanol, showing high methanol tolerance activity.

system with *Ibam* space group. Parallel chains of edge-sharing $CoSe_{4/2}$ tetrahedra run along [0, 0, 1] and [1/2, 1/2, 1] as shown in Figure S1.[53] Co occupies tetrahedral voids formed by Se, and Pd atom is surrounded by five Se atoms in a distorted quadratic−prismatic arrangement. Since both of the active sites are encapsulated within the Se cage, thus, the active sites are expected to have protection from poisoning intermediates.

Oleylamine used during the synthesis not only can act as a solvent and a surfactant but can also act as an electron donor at elevated temperature.[54] Trioctylphosphine (TOP) acts as a stabilizing agent and prevents agglomeration of nanoparticles.[55] Adjusting the ratio between them results in well-separated nanoparticles with intermediate particle size.[56]

Rietveld refinement of the experimental PXRD pattern in Figure 1a and Fourier transformed Pd and Se *k*-edge XAFS data (Figure S2) confirm the purity of the phase. The PXRD pattern could be indexed as orthorhombic with *Ibam* space group and lattice parameters a = 5.993 Å, b = 10.493 Å, and c = 5.003 Å. Comparison of the Se *k*-edge XANES spectra (Figure 1b) with reference Se foil (zero oxidation state) and CoSe and NiSe (−2 oxidation state) indicates that the Se in the compound has a partial negative oxidation state. XPS spectra of individual elements are presented in Figure S3. STEM and elemental mapping in Figure 1c confirm the homogeneous distribution of elements throughout. The FESEM images in Figure 1d show a well-defined morphology of particles. The EDAX composition is presented in Figure S4.

The TEM image shows that the nanoparticles are less than 100 nm in size (Figure 1e). At first sight, these particles seem to have different morphologies. However, BFDH morphology simulation of the nanocrystals, followed by spatial orientation along a different direction, shows morphology similar to that obtained in the TEM image (Figure 1f). Only four sets of planes (002), ($1\bar{2}1$), (110), and ($0\bar{2}0$) are found to contribute to this morphology (Table S1).

3.2. Activity. The glassy carbon modified electrode was first activated prior to RDE measurements in N_2-saturated 0.1 M KOH solution (Figure S5a). To obtain a stable current density, 100 CV activation cycles were performed. To evaluate the ORR catalytic activity of $CoPd_2Se_2$, the linear sweep voltammetry curves were then recorded in O_2-saturated 0.1 M KOH solution, at a scan rate of 5 mV s^{-1}. The polarization curves for ORR at different rotation rates are shown in Figure S5b in which current densities are normalized with respect to the geometrical surface area (0.0706 cm^2). The catalyst exhibits current density of 1 mA cm^{-2} at a potential of 0.94 V vs RHE compared to Pd/C (0.90 V) and Pt/C (0.93 V). However, after an initial cycling of 1000 cycles using RRDE, $CoPd_2Se_2$ showed negligible change in the potential, suggesting extraordinary stability similar to the state-of-the-art catalysts Pt/C and Pd/C (Figure 2a). The nature of Pt/C and Pd/C polarization curve corroborates well with the previous literature results.[57−59]

The activity of the catalyst was also checked for OER in 0.1 M KOH. The catalyst was found to show good activity compared to state-of-the-art RuO_2/C (Figure S6). The potential gap between the OER and ORR process, taken at the current densities of 10 and −3 mA cm^{-2}, respectively, was found to be $\Delta E = E_{OER@10} - E_{ORR@-3}$ = 829 mV. Further study on OER was not performed as the present study completely focuses on the ORR aspect of the catalyst.

3.3. Durability Test and Kinetics Study for $CoPd_2Se_2$. A durability test was performed to assess their ability to sustain activity as shown in Figure 2b. Cyclic potential sweeps were performed between 0.4 and 0.9 V vs RHE, at a scan rate of 0.1 V/s and a rotation speed of 800 rpm in O_2-saturated 0.1 M KOH. An accelerated degradation test (ADT) was performed using RDE working electrodes with 3 mm diameter and graphite rod (purity > 99.9%, Sigma-Aldrich) as the counter electrode to avoid Pt dissolution. After 50000 cycles, the half-wave potential of $CoPd_2Se_2$ remains high with a slight negative shift in the mixed kinetic−diffusion limited region. Tafel plots were plotted to understand the kinetics of the catalyst. The Tafel slope obtained toward the ORR before cycling was 56.2 mV dec^{-1} at lower overpotential, which decreased to 46.5 mV dec^{-1} (Figure 2c). This Tafel slope value indicates that, during the initial reaction, the oxygen reduction, catalyzed by the $CoPd_2Se_2$ chalcogenide, is controlled by the first charge-transfer step, similar to that of the state-of-the-art Pt catalyst. During the course of the reaction, a value close to 40 mV dec^{-1} indicates the dissociation of O═O as the rate-determining step.[60]

Methanol tolerance test was performed to check the stability of the catalyst in the case of fuel crossover in a fuel cell. Linear-sweep voltammetry was run in the presence of 1 M methanol, keeping all of the experimental parameters the same (Figure

DOI: 10.1021/acsaem.9b01400
ACS Appl. Energy Mater. 2020, 3, 231−239

2d). However, no significant change in the nature of the curve was observed even after the addition of methanol. The Tafel slope value also remains almost unaffected by the addition of methanol (Figure 2e). Chronoamperometric measurements were carried out for 50000 s to further test the durability of the catalyst (Figure S7).

As seen from Figure S8, the size of the particle grows with the number of cycles. This may be due to electrochemical sintering of the nanoparticles. However, the homogeneity of the particles remained intact even after 30 K cycles (Figure S9). It was tough to do elemental mapping on the particles after 50 K as the surface was enriched with Se and the electron beam damaged the surface (Figure S10). So, FESEM-EDAX images were collected as shown in Figure S11.

3.4. Selectivity toward H_2O Pathway. The plot of $1/j$ vs $\omega^{-1/2}$ for the potential range of 0.1−0.6 V (vs RHE) yields a series of essentially parallel straight lines, having a slope value of B. The linearity and parallelism of all lines in Figure S5c indicate that the electron number transferred per oxygen molecule and the active surface area of the catalyst do not obviously change in the potential range measured. A value of $n \sim 4$ is obtained for the catalyst $CoPd_2Se_2$, unlike Co−Se and $CoSe_2$/C which have values of n = 3.4 and 3.5, respectively.[61] To further confirm the selectivity toward H_2O, RRDE measurement was carried out following the same experimental procedure. The percentage of H_2O_2 produced and the number of electrons consumed during the reaction were recorded before and after 1000 cycles (Figure 2) and tabulated in Table S2.

To demonstrate the efficiency of our catalyst, state-of-the-art catalysts Pd/C (20 wt %) and Pt/C (20 wt %) were used as the references. The percentage of H_2O_2 produced in the case of $CoPd_2Se_2$ is less than 3.5% during the first cycle, which is comparable to that of Pt/C (∼2.5%) and much better compared to Pd/C (∼13%). However, after 1000 cycles, the percentage of H_2O_2 produced on Pt/C, across the entire potential range, is higher than that of $CoPd_2Se_2$. Thus, $CoPd_2Se_2$ exhibits very high selectivity toward H_2O over a wide potential range.

For achieving high energy efficiency, $4e^-$ reduction to H_2O is important. This is possible only when O_2 adsorbs side-on in a bridge site of a strongly adsorbing atom. However, strong O adsorption can pose a challenge for the stability of the catalyst. This is clearly seen in state-of-the-art catalyst Pt/C which exhibits superior activity but undergoes degradation due to active site poisoning by strongly adsorbing -OH intermediates. Thus, designing a catalyst with both good activity and good stability remains a challenge. Given the oxophilic character of Co and Pd active sites, Se is necessary to act as a sacrificially protective agent. In a similar system, we have recently found that the Se−Se coordination number decreases during electrochemical ORR, which is due to Se occupying edges and surfaces due to its lower surface energy (0.10 J/m^2) compared to Co (2.34 J/m^2) and Pd (1.43 J/m^2).[20]

Using density functional theory (DFT), we calculated the adsorption energy of ORR intermediates on the (100) plane (taken as a representative plane) (Figure S12). The binding energies for the systems under consideration were obtained from

$$\Delta E_b = E(\text{ads/slab}) - E(\text{slab}) - E(\text{ads})$$

where E(ads/slab) is the energy of the final optimized adsorption configuration on the slab, E(ads) is the energy of the adsorbed molecule, and E(slab) is the energy of the catalyst surface. With this definition, a negative ΔE_b value corresponds to a stable adsorption on the surface.

Sites A−G in Figure 3a represent various adsorption sites of O_2 on the $CoPd_2Se_2$ surface. Since $4e^-$ dissociation of O_2 is

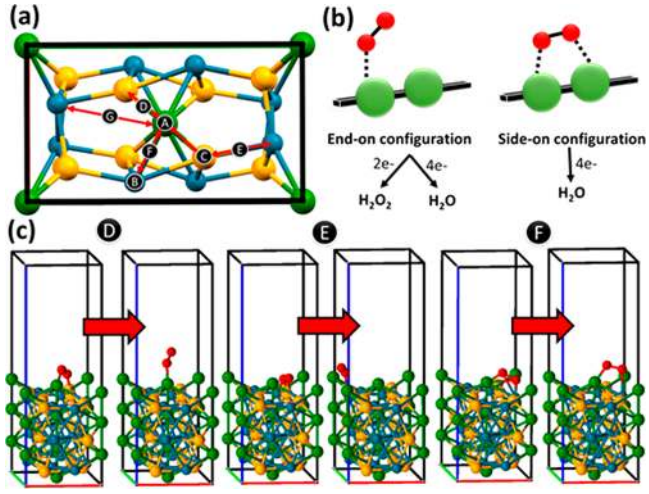

Figure 3. (a) Adsorption of O_2 molecule on probable adsorption sites, (b) end-on and side-on adsorption configuration of O_2 molecule and (c) DFT structural input and output configuration of O_2 adsorbing on site **D**, **E** and **F**. Green, yellow, blue and red atom represents Co, Se, Pd and O atom, respectively.

observed using an electrochemical K−L plot. Thus, it is expected that the molecule adsorbs side-on instead of end-on (Figure 3b). Henceforth, A−C adsorption sites can be ignored due to end-on adsorption on these sites.

Adsorption energy of the O_2 adsorbate is listed in Table 1. We observe that O_2 molecule has higher negative adsorption

Table 1. O_2 Adsorption Energies and Optimized Bond Lengths of O−O and M−O Bonds

adsorption site	adsorption energy (eV)	d_{o-o} (Å)	d_{co-O} (Å)	d_{PD-O} (Å)
site F	−3.032	1.338	1.724	2.146
site G	−2.845	3.612	1.649	2.069

energy when adsorbed on site F (−3.032 eV) compared to that on site G (−2.845 eV). However, complete dissociation of O_2 molecule takes place on site G (d_{O-O} = 3.612 Å) unlike on site F (d_{O-O} = 1.338 Å) as shown in Figure 4a. Since the adsorption energy is calculated wrt the O_2 molecule, we ignored the energy of dissociation which is consumed during the process. An energy of 8.75 eV is wasted to dissociate an O_2 molecule to its corresponding atom. Adding this energy gives a more stable adsorption (−11.59 eV) on site G compared to site F. Free energy of H_2O on the catalyst surface was calculated to be 0.04 eV, indicating easy desorption of the H_2O formed.

Thus, we use the bridge site G, having a Co−Pd bond distance of 4.496 Å, as a descriptor for a stable adsorption site for O_2 dissociation. As seen in Figure 4c, all of the planes obtained by BFDH morphology calculation have a high density of active site G represented by red arrows. Thus, complete dissociation of O_2 molecule to O and complete $4e^-$ reduction of O_2 are expected.

DOI: 10.1021/acsaem.9b01400
ACS Appl. Energy Mater. 2020, 3, 231−239

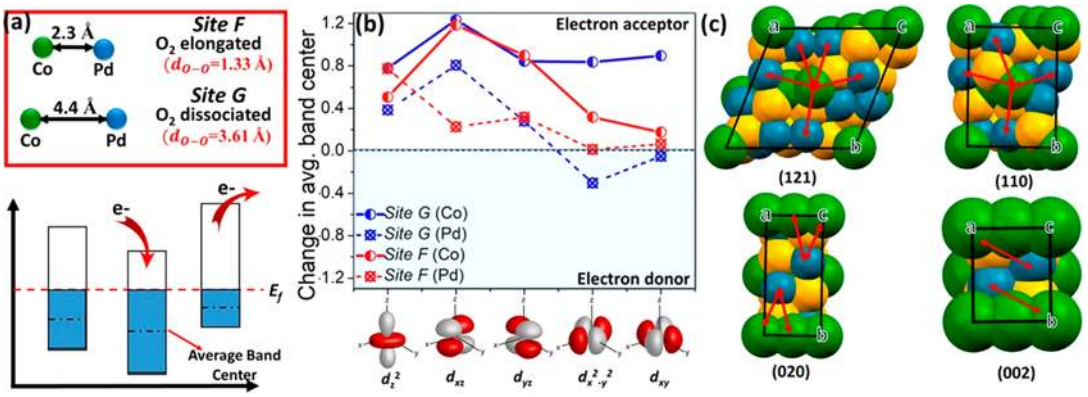

Figure 4. (a) Schematic presentation of site F and site G and change in the average band center when adsorbate withdraws or donates electron density, (b) plot of average band center for all of the orbitals of each adsorption site, and (c) high density of site G in the planes obtained from BFDH morphology calculation.

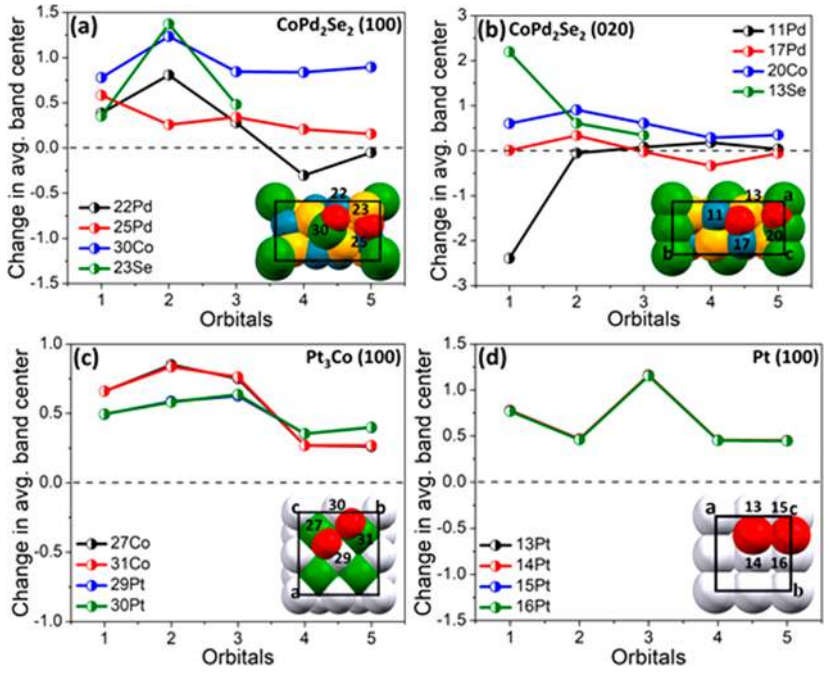

Figure 5. Change in average band center for O_2 adsorption site in (a) (100) and (b) (020) planes of $CoPd_2Se_2$. The trend is compared with that of the (100) plane of (c) Pt_3CO and (d) Pt. Green, yellow, blue, white, and red atoms represent Co, Se, Pd, Pt, and O atoms, respectively. Orbitals 1−5 represent d_{z^2}, d_{xz}, d_{yz}, $d_{x^2-y^2}$, and d_{xy} orbitals for d-shell and p_z, p_x, and p_y orbitals for p-shell (in sequential order).

Due to shortened M−O bond length, it is expected that π orbital on oxygen molecule interacts strongly with the d orbital of the transition metal and increased O═O bond length confirms that there is substantial back-donation from filled d-orbitals to the empty π^* antibonding orbital of the molecule. Thus, a detailed analysis on the PDOS of corresponding metal sites was requisite to understand the role of each metal site (Co and Pd). Since site G was chosen as the descriptor for the other planes, so a detailed PDOS analysis was done on Co and Pd active sites as shown in Figure 4b.

A change in the average band center was recorded for each of the metal orbitals of the adsorbing atom (Table S3). A positive change signifies an electron acceptance, and a negative change is indicative of the electron donation of the orbitals. Figure 5 clearly demonstrates that all of the Co d orbitals played the role of accepting electron density from the π orbital of the oxygen molecule, thus forming a strong Co−O bond. However, few of the d orbitals of Pd (d_{z^2}, d_{xz}, d_{yz}) acted as an electron acceptor, and some of these orbitals ($d_{x^2-y^2}$ and d_{xy}) back-donated to the empty π^* antibonding orbital of the molecule. Thus, Pd formed a strong Pd−O bond and also played a vital role in dissociating the O_2 molecule. Site F was unable to dissociate the O_2 molecule due to insufficient back-donation from only $d_{x^2-y^2}$ orbital. Since O_2 adsorbs side-on and better fits into the hollow site G, so it is expected that it interacts strongly with the back-donating $d_{x^2-y^2}$ and d_{xy} orbitals, which is not possible in the case of site F. Mismatch in the spatial overlap of the orbitals in adsorbate and adsorbant rationalizes the elongation of O_2 on site F and complete dissociation on site G. The operating mechanism of $CoPd_2Se_2$ is found to be different than those of Pt and Pt_3Co (taken as references). The positive change in the average band center in these reference compounds indicates weakening of the O═O bond through strong electron acceptance from O_2. Thus, Co weakens the O═O bond through strongly interacting with one of the O atoms and Pd weakens through strong interaction and

DOI: 10.1021/acsaem.9b01400
ACS Appl. Energy Mater. 2020, 3, 231−239

back-donation of electron density. Se provides necessary protection to the active sites from poisoning intermediates. The role of each element is thus deconvoluted and can be used to design and improve the selectivity of O_2 catalyst toward H_2O or H_2O_2 products.

4. CONCLUSION

In conclusion, a ternary metal chalcogenide catalyst for oxygen reduction was synthesized by colloidal synthesis method for the first time, which demonstrated significantly high ORR activity, stability, and selectivity. Detailed insight into the roles of Co, Pd, and Se gained both by experiment and from DFT calculations may possibly inspire logical designing of catalyst with a better figure of merit. Our study also highlights the important aspect of alloying and shape-tailoring to control the exposed crystallographic facet of the catalysts to enhance the ORR performance and hence to develop more advanced non-Pt-based electrocatalysts. The strategy demonstrated here can be extended to design and develop the other Pd-based highly active and robust electrocatalysts in the field of electrocatalysis.

■ ASSOCIATED CONTENT

Supporting Information

The Supporting Information is available free of charge at https://pubs.acs.org/doi/10.1021/acsaem.9b01400.

Experimental details, tables, crystal structure, XANES, XPS, EDAX, LSV polarization curve, chronoamperometeric curve, TEM, and adsorption configuration of various ORR intermediates (PDF)

■ AUTHOR INFORMATION

Corresponding Author

*E-mail: sebastiancp@jncasr.ac.in.

ORCID

Saurav Ch. Sarma: 0000-0002-6941-9702
Vidyanshu Mishra: 0000-0002-8660-2859
Sebastian C. Peter: 0000-0002-5211-446X

Notes

The authors declare no competing financial interest.

■ ACKNOWLEDGMENTS

Financial support from the Department of Science and Technology [Hydrogen and Fuel Cell - 2018 Scheme with Grant No.DST/TMD/HFC/2K18/128(G)], Sheikh Saqr Laboratory, Jawaharlal Nehru Centre for Advanced Scientific Research (JNCASR) and the Technical Research Centre (TRC) in JNCASR (JNC/AO/DST-TRC/C.14.10/16.2750) is gratefully acknowledged. Parts of this research were also carried out at the light source PETRA III at DESY, a member of the Helmholtz Association (HGF), and we thank Dr. Edmund Welter for assistance in using PETRA III beamline P65 at DESY, Germany. We also thank DST for financial assistance for the measurement at DESY. We are grateful to Prof. C. N. R. Rao for his constant support and encouragement.

■ REFERENCES

(1) Shao, M. H.; Huang, T.; Liu, P.; Zhang, J.; Sasaki, K.; Vukmirovic, M. B.; Adzic, R. R. Palladium Monolayer and Palladium Alloy Electrocatalysts for Oxygen Reduction. *Langmuir* **2006**, *22* (25), 10409−10415.

(2) Shao, Y.; Zhang, S.; Wang, C.; Nie, Z.; Liu, J.; Wang, Y.; Lin, Y. Highly durable graphene nanoplatelets supported Pt nanocatalysts for oxygen reduction. *J. Power Sources* **2010**, *195* (15), 4600−4605.

(3) Wang, J.; Chen, Y.; Liu, H.; Li, R.; Sun, X. Synthesis of Pd nanowire networks by a simple template-free and surfactant-free method and their application in formic acid electrooxidation. *Electrochem. Commun.* **2010**, *12* (2), 219−222.

(4) Wen, Z.; Liu, J.; Li, J. Core/Shell Pt/C Nanoparticles Embedded in Mesoporous Carbon as a Methanol-Tolerant Cathode Catalyst in Direct Methanol Fuel Cells. *Adv. Mater.* **2008**, *20* (4), 743−747.

(5) Huo, R.; Jiang, W.-J.; Xu, S.; Zhang, F.; Hu, J.-S. Co/CoO/$CoFe_2O_4$/G nanocomposites derived from layered double hydroxides towards mass production of efficient Pt-free electrocatalysts for oxygen reduction reaction. *Nanoscale* **2014**, *6* (1), 203−206.

(6) Wei, Z. D.; Chan, S. H.; Li, L. L.; Cai, H. F.; Xia, Z. T.; Sun, C. X. Electrodepositing Pt on a Nafion-bonded carbon electrode as a catalyzed electrode for oxygen reduction reaction. *Electrochim. Acta* **2005**, *50* (11), 2279−2287.

(7) Sarma, S. C.; Peter, S. C. Understanding small-molecule electro-oxidation on palladium based compounds − a feature on experimental and theoretical approaches. *Dalton Trans.* **2018**, *47* (24), 7864−7869.

(8) Sarma, S. C.; Mishra, V.; Ann Mary, K. A.; Roy, S.; Peter, S. C. Inverse Strain Effect in Atomic Scale"—Enhanced Hydrogen Evolution Activity and Durability in Cu-Substituted Palladseite. *ACS Energy Lett.* **2018**, *3*, 3008−3014.

(9) Sarma, S. C.; Subbarao, U.; Khulbe, Y.; Jana, R.; Peter, S. C. Are we underrating rare earths as an electrocatalyst? The effect of their substitution in palladium nanoparticles enhances the activity towards ethanol oxidation reaction. *J. Mater. Chem. A* **2017**, *5* (44), 23369−23381.

(10) McLean, G. F.; Niet, T.; Prince-Richard, S.; Djilali, N. An assessment of alkaline fuel cell technology. *Int. J. Hydrogen Energy* **2002**, *27* (5), 507−526.

(11) Kinoshita, K.; Electrochemical, S. *Electrochemical oxygen technology*. Wiley: New York, 1992.

(12) Morallón, E.; Vázquez, J. L.; Aldaz, A. Electrochemical behaviour of Pt(111) in alkaline media. Effect of specific adsorption of anions. *J. Electroanal. Chem.* **1992**, *334* (1−2), 323−338.

(13) Spendelow, J. S.; Wieckowski, A. Electrocatalysis of oxygen reduction and small alcohol oxidation in alkaline media. *Phys. Chem. Chem. Phys.* **2007**, *9* (21), 2654−2675.

(14) Wang, K.; Wang, Y.; Tong, Y.; Pan, Z.; Song, S. A Robust Versatile Hybrid Electrocatalyst for the Oxygen Reduction Reaction. *ACS Appl. Mater. Interfaces* **2016**, *8* (43), 29356−29364.

(15) Park, J.; Kanti Kabiraz, M.; Kwon, H.; Park, S.; Baik, H.; Choi, S.-I.; Lee, K. Radially Phase Segregated PtCu@PtCuNi Dendrite@Frame Nanocatalyst for the Oxygen Reduction Reaction. *ACS Nano* **2017**, *11* (11), 10844−10851.

(16) Deng, Y.; Xue, H.; Lu, S.; Song, Y.; Cao, X.; Wang, L.; Wang, H.; Zhao, Y.; Gu, H. Trimetallic Au@PtPd Mesoporous Nanorods as Efficient Electrocatalysts for the Oxygen Reduction Reaction. *ACS Appl. Energy Mater.* **2018**, *1* (9), 4891−4898.

(17) Lin, L.; Yang, Z. K.; Jiang, Y.-F.; Xu, A.-W. Nonprecious Bimetallic (Fe, Mo)−N/C Catalyst for Efficient Oxygen Reduction Reaction. *ACS Catal.* **2016**, *6* (7), 4449−4454.

(18) Shen, Y.; Shi, D.; Liu, L.; Liao, F.; Zhu, W.; Shao, M. Pd Nanoparticles/F, N Codoping Graphene Composites for Oxygen Reduction and Zinc-Air Batteries. *ACS Sustainable Chem. Eng.* **2019**, *7* (14), 12281−12287.

(19) Ramaswamy, N.; Allen, R. J.; Mukerjee, S. Electrochemical Kinetics and X-ray Absorption Spectroscopic Investigations of Oxygen Reduction on Chalcogen-Modified Ruthenium Catalysts in Alkaline Media. *J. Phys. Chem. C* **2011**, *115* (25), 12650−12664.

(20) Sarma, S. C.; Vemuri, V.; Mishra, V.; Peter, S. C. Sacrificial protection in action!": ultra-high stability of palladesite mineral towards the oxygen reduction reaction. *J. Mater. Chem. A* **2019**, *7* (3), 979−984.

(21) Rosli, N. F.; Mayorga-Martinez, C. C.; Latiff, N. M.; Rohaizad, N.; Sofer, Z.; Fisher, A. C.; Pumera, M. Layered $PtTe_2$ Matches

DOI: 10.1021/acsaem.9b01400
ACS Appl. Energy Mater. 2020, 3, 231−239

Electrocatalytic Performance of Pt/C for Oxygen Reduction Reaction with Significantly Lower Toxicity. *ACS Sustainable Chem. Eng.* **2018**, *6* (6), 7432−7441.
(22) Tang, C.; Pu, Z.; Liu, Q.; Asiri, A. M.; Sun, X. NiS_2 nanosheets array grown on carbon cloth as an efficient 3D hydrogen evolution cathode. *Electrochim. Acta* **2015**, *153*, 508−514.
(23) Faber, M. S.; Dziedzic, R.; Lukowski, M. A.; Kaiser, N. S.; Ding, Q.; Jin, S. High-Performance Electrocatalysis Using Metallic Cobalt Pyrite (CoS_2) Micro- and Nanostructures. *J. Am. Chem. Soc.* **2014**, *136* (28), 10053−10061.
(24) Wang, H. L.; Liang, Y. Y.; Li, Y. G.; Dai, H. J. $Co_{1-x}S$-Graphene Hybrid: A High-Performance Metal Chalcogenide Electrocatalyst for Oxygen Reduction. *Angew. Chem., Int. Ed.* **2011**, *50* (46), 10969−10972.
(25) Feng, Y.; He, T.; Alonso-Vante, N. In situ Free-Surfactant Synthesis and ORR- Electrochemistry of Carbon-Supported Co_3S_4 and $CoSe_2$ Nanoparticles. *Chem. Mater.* **2008**, *20* (1), 26−28.
(26) Cao, X.; Zheng, X.; Tian, J.; Jin, C.; Ke, K.; Yang, R. Cobalt Sulfide Embedded in Porous Nitrogen-doped Carbon as a Bifunctional Electrocatalyst for Oxygen Reduction and Evolution Reactions. *Electrochim. Acta* **2016**, *191*, 776−783.
(27) Kong, D.; Wang, H.; Lu, Z.; Cui, Y. $CoSe_2$ Nanoparticles Grown on Carbon Fiber Paper: An Efficient and Stable Electrocatalyst for Hydrogen Evolution Reaction. *J. Am. Chem. Soc.* **2014**, *136* (13), 4897−4900.
(28) Liu, Q.; Shi, J.; Hu, J.; Asiri, A. M.; Luo, Y.; Sun, X. $CoSe_2$ Nanowires Array as a 3D Electrode for Highly Efficient Electrochemical Hydrogen Evolution. *ACS Appl. Mater. Interfaces* **2015**, *7* (7), 3877−3881.
(29) Zhang, H.; Lei, L.; Zhang, X. One-step synthesis of cubic pyrite-type $CoSe_2$ at low temperature for efficient hydrogen evolution reaction. *RSC Adv.* **2014**, *4* (97), 54344−54348.
(30) Masud, J.; Nath, M. Co_7Se_8 Nanostructures as Catalysts for Oxygen Reduction Reaction with High Methanol Tolerance. *ACS Energy Lett.* **2016**, *1* (1), 27−31.
(31) Radhakrishnan, T.; Aparna, M. P.; Chatanathodi, R.; Sandhyarani, N. Amorphous Rhenium Disulfide Nanosheets: A Methanol-Tolerant Transition Metal Dichalcogenide Catalyst for Oxygen Reduction Reaction. *ACS Appl. Nano Mater.* **2019**, *2* (7), 4480−4488.
(32) Chhowalla, M.; Shin, H. S.; Eda, G.; Li, L.-J.; Loh, K. P.; Zhang, H. The chemistry of two-dimensional layered transition metal dichalcogenide nanosheets. *Nat. Chem.* **2013**, *5* (4), 263−275.
(33) Chen, S.; Duan, J.; Tang, Y.; Jin, B.; Zhang Qiao, S. Molybdenum sulfide clusters-nitrogen-doped graphene hybrid hydrogel film as an efficient three-dimensional hydrogen evolution electrocatalyst. *Nano Energy* **2015**, *11*, 11−18.
(34) Wang, H.; Lu, Z.; Kong, D.; Sun, J.; Hymel, T. M.; Cui, Y. Electrochemical Tuning of MoS_2 Nanoparticles on Three-Dimensional Substrate for Efficient Hydrogen Evolution. *ACS Nano* **2014**, *8* (5), 4940−4947.
(35) Duan, J. J.; Chen, S.; Chambers, B. A.; Andersson, G. G.; Qiao, S. Z. 3D WS_2 Nanolayers@Heteroatom-Doped Graphene Films as Hydrogen Evolution Catalyst Electrodes. *Adv. Mater.* **2015**, *27* (28), 4234−4241.
(36) Chua, X. J.; Luxa, J.; Eng, A. Y. S.; Tan, S. M.; Sofer, Z.; Pumera, M. Negative Electrocatalytic Effects of p-Doping Niobium and Tantalum on MoS_2 and WS_2 for the Hydrogen Evolution Reaction and Oxygen Reduction Reaction. *ACS Catal.* **2016**, *6* (9), 5724−5734.
(37) Srejic, I.; Rakocevic, Z.; Nenadovic, M.; Strbac, S. Oxygen reduction on polycrystalline palladium in acid and alkaline solutions: topographical and chemical Pd surface changes. *Electrochim. Acta* **2015**, *169*, 22−31.
(38) Wang, S.; Chu, X.; Zhang, X.; Zhang, Y.; Mao, J.; Yang, Z. A First-Principles Study of O2 Dissociation on Platinum Modified Titanium Carbide: A Possible Efficient Catalyst for the Oxygen Reduction Reaction. *J. Phys. Chem. C* **2017**, *121* (39), 21333−21342.
(39) Suo, Y.; Zhuang, L.; Lu, J. First-Principles Considerations in the Design of Pd-Alloy Catalysts for Oxygen Reduction. *Angew. Chem., Int. Ed.* **2007**, *46* (16), 2862−2864.
(40) Bu, L.; Zhang, N.; Guo, S.; Zhang, X.; Li, J.; Yao, J.; Wu, T.; Lu, G.; Ma, J.-Y.; Su, D.; Huang, X. Biaxially strained PtPb/Pt core/shell nanoplate boosts oxygen reduction catalysis. *Science* **2016**, *354* (6318), 1410−1414.
(41) Shi, Z.; Zhang, J.; Liu, Z.-S.; Wang, H.; Wilkinson, D. P. Current status of ab initio quantum chemistry study for oxygen electroreduction on fuel cell catalysts. *Electrochim. Acta* **2006**, *51* (10), 1905−1916.
(42) Choi, C. H.; Kwon, H. C.; Yook, S.; Shin, H.; Kim, H.; Choi, M. Hydrogen Peroxide Synthesis via Enhanced Two-Electron Oxygen Reduction Pathway on Carbon-Coated Pt Surface. *J. Phys. Chem. C* **2014**, *118* (51), 30063−30070.
(43) Sun, Y.; Sinev, I.; Ju, W.; Bergmann, A.; Dresp, S.; Kühl, S.; Spöri, C.; Schmies, H.; Wang, H.; Bernsmeier, D.; Paul, B.; Schmack, R.; Kraehnert, R.; Roldan Cuenya, B.; Strasser, P. Efficient Electrochemical Hydrogen Peroxide Production from Molecular Oxygen on Nitrogen-Doped Mesoporous Carbon Catalysts. *ACS Catal.* **2018**, *8* (4), 2844−2856.
(44) Nikitenko, S.; Beale, A. M.; van der Eerden, A. M. J.; Jacques, S. D. M.; Leynaud, O.; O'Brien, M. G.; Detollenaere, D.; Kaptein, R.; Weckhuysen, B. M.; Bras, W. Implementation of a combined SAXS/WAXS/QEXAFS set-up for time-resolved in situ experiments. *J. Synchrotron Radiat.* **2008**, *15*, 632−640.
(45) Ravel, B.; Newville, M. ATHENA, ARTEMIS, HEPHAESTUS: data analysis for X-ray absorption spectroscopy using IFEFFIT. *J. Synchrotron Radiat.* **2005**, *12*, 537−541.
(46) Feng, Y.; Shao, Q.; Ji, Y.; Cui, X.; Li, Y.; Zhu, X.; Huang, X. Surface-modulated palladium-nickel icosahedra as high-performance non-platinum oxygen reduction electrocatalysts. *Sci. Adv.* **2018**, *4* (7), No. eaap8817.
(47) Tong, X.; Zhang, J.; Zhang, G.; Wei, Q.; Chenitz, R.; Claverie, J. P.; Sun, S. Ultrathin Carbon-Coated Pt/Carbon Nanotubes: A Highly Durable Electrocatalyst for Oxygen Reduction. *Chem. Mater.* **2017**, *29* (21), 9579−9587.
(48) Escudero-Escribano, M.; Verdaguer-Casadevall, A.; Malacrida, P.; Grønbjerg, U.; Knudsen, B. P.; Jepsen, A. K.; Rossmeisl, J.; Stephens, I. E. L.; Chorkendorff, I. Pt_5Gd as a Highly Active and Stable Catalyst for Oxygen Electroreduction. *J. Am. Chem. Soc.* **2012**, *134* (40), 16476−16479.
(49) Giannozzi, P.; Baroni, S.; Bonini, N.; Calandra, M.; Car, R.; Cavazzoni, C.; Ceresoli, D.; Chiarotti, G. L; Cococcioni, M.; Dabo, I.; Dal Corso, A.; de Gironcoli, S.; Fabris, S.; Fratesi, G.; Gebauer, R.; Gerstmann, U.; Gougoussis, C.; Kokalj, A.; Lazzeri, M.; Martin-Samos, L.; Marzari, N.; Mauri, F.; Mazzarello, R.; Paolini, S.; Pasquarello, A.; Paulatto, L.; Sbraccia, C.; Scandolo, S.; Sclauzero, G.; Seitsonen, A. P; Smogunov, A.; Umari, P.; Wentzcovitch, R. M QUANTUM ESPRESSO: a modular and open-source software project for quantum simulations of materials. *J. Phys.: Condens. Matter* **2009**, *21* (39), 395502.
(50) Perdew, J. P.; Burke, K.; Ernzerhof, M. Generalized Gradient Approximation Made Simple. *Phys. Rev. Lett.* **1996**, *77* (18), 3865−3868.
(51) Hammer, B.; Norskov, J. K. Electronic factors determining the reactivity of metal surfaces. *Surf. Sci.* **1995**, *343* (3), 211−220.
(52) Vielhaber, E.; Hoppe, R. Zur Kristallstruktur von K_2ZnO_2. *Z. Anorg. Allg. Chem.* **1968**, *360* (1−2), 7−14.
(53) Pocha, R.; Lohnert, C.; Johrendt, D. The metal-rich palladium chalcogenides Pd_2MCh_2 (M = Fe, Co, Ni; Ch = Se, Te): Crystal structure and topology of the electron density. *J. Solid State Chem.* **2007**, *180* (1), 191−197.
(54) Mourdikoudis, S.; Liz-Marzan, L. M. Oleylamine in Nanoparticle Synthesis. *Chem. Mater.* **2013**, *25* (9), 1465−1476.
(55) Chen, Y. Z.; Luo, X. H.; Yue, G. H.; Luo, X. T.; Peng, D. L. Synthesis of iron-nickel nanoparticles via a nonaqueous organometallic route. *Mater. Chem. Phys.* **2009**, *113* (1), 412−416.

DOI: 10.1021/acsaem.9b01400
ACS Appl. Energy Mater. 2020, 3, 231−239

(56) Carenco, S.; Boissiere, C.; Nicole, L.; Sanchez, C.; Le Floch, P.; Mezailles, N. Controlled Design of Size-Tunable Monodisperse Nickel Nanoparticles. *Chem. Mater.* **2010**, *22* (4), 1340−1349.
(57) Ge, X.; Sumboja, A.; Wuu, D.; An, T.; Li, B.; Goh, F. W. T.; Hor, T. S. A.; Zong, Y.; Liu, Z. Oxygen Reduction in Alkaline Media: From Mechanisms to Recent Advances of Catalysts. *ACS Catal.* **2015**, *5* (8), 4643−4667.
(58) Jiang, K.; Wang, P.; Guo, S.; Zhang, X.; Shen, X.; Lu, G.; Su, D.; Huang, X. Ordered PdCu-Based Nanoparticles as Bifunctional Oxygen-Reduction and Ethanol-Oxidation Electrocatalysts. *Angew. Chem., Int. Ed.* **2016**, *55* (31), 9030−9035.
(59) Huang, H.; Li, K.; Chen, Z.; Luo, L.; Gu, Y.; Zhang, D.; Ma, C.; Si, R.; Yang, J.; Peng, Z.; Zeng, J. Achieving Remarkable Activity and Durability toward Oxygen Reduction Reaction Based on Ultrathin Rh-Doped Pt Nanowires. *J. Am. Chem. Soc.* **2017**, *139* (24), 8152−8159.
(60) Shinagawa, T.; Garcia-Esparza, A. T.; Takanabe, K. Insight on Tafel slopes from a microkinetic analysis of aqueous electrocatalysis for energy conversion. *Sci. Rep.* **2015**, *5*, 13801.
(61) Feng, Y.; He, T.; Alonso-Vante, N. Oxygen reduction reaction on carbon-supported $CoSe_2$ nanoparticles in an acidic medium. *Electrochim. Acta* **2009**, *54* (22), 5252−5256.

DOI: 10.1021/acsaem.9b01400
ACS Appl. Energy Mater. 2020, 3, 231−239